Article

The Precipitation Imaging Package: Phase Partitioning Capabilities

Claire Pettersen [1,*], Larry F. Bliven [2], Mark S. Kulie [3], Norman B. Wood [1], Julia A. Shates [4], Jaclyn Anderson [5], Marian E. Mateling [4], Walter A. Petersen [6], Annakaisa von Lerber [7] and David B. Wolff [2]

1   Space Science and Engineering Center, University of Wisconsin–Madison, Madison, WI 53706, USA; norman.wood@ssec.wisc.edu
2   NASA Goddard Space Flight Center, Wallops Flight Facility, Wallops Island, VA 23337, USA; francis.l.bliven@nasa.gov (L.F.B.); david.b.wolff@nasa.gov (D.B.W.)
3   Advanced Satellite Products Branch, NOAA/NESDIS/Center for Satellite Applications and Research, Madison, WI 53706, USA; mark.kulie@noaa.gov
4   Department of Atmospheric and Oceanic Sciences, University of Wisconsin–Madison, Madison, WI 53706, USA; shates@wisc.edu (J.A.S.); mateling@wisc.edu (M.E.M.)
5   National Weather Service, NOAA, Milwaukee, WI 53118, USA; jaclyn.anderson@noaa.gov
6   NASA Marshall Space Flight Center, Huntsville, AL 35808, USA; walt.petersen@nasa.gov
7   Finnish Meteorological Institute, 00560 Helsinki, Finland; Annakaisa.von.Lerber@fmi.fi
*   Correspondence: claire.pettersen@ssec.wisc.edu

Abstract: Surface precipitation phase is a fundamental meteorological property with immense importance. Accurate classification of phase from satellite remotely sensed observations is difficult. This study demonstrates the ability of the Precipitation Imaging Package (PIP), a ground-based, in situ precipitation imager, to distinguish precipitation phase. The PIP precipitation phase identification capabilities are compared to observer records from the National Weather Service (NWS) office in Marquette, Michigan, as well as co-located observations from profiling and scanning radars, disdrometer data, and surface meteorological measurements. Examined are 13 events with at least one precipitation phase transition. The PIP-determined onsets and endings of the respective precipitation phase periods agree to within 15 min of NWS observer records for the vast majority of the events. Additionally, the PIP and NWS liquid water equivalent accumulations for 12 of the 13 events were within 10%. Co-located observations from scanning and profiling radars, as well as reanalysis-derived synoptic and thermodynamic conditions, support the accuracy of the precipitation phases identified by the PIP. PIP observations for the phase transition events are compared to output from a parameterization based on wet bulb and near-surface lapse rates to produce a probability of solid precipitation. The PIP phase identification and the parameterization output are consistent. This work highlights the ability of the PIP to properly characterize hydrometeor phase and provide dependable precipitation accumulations under complicated mixed-phase and rain and snow (or vice versa) transition events.

Keywords: precipitation; mixed-phase precipitation; rain rate; snowfall rate; snow mass retrieval; video disdrometers

1. Introduction

The phase of surface precipitation is a fundamental meteorological property with immense importance. Transitions between liquid, solid, and mixed-phase precipitation at a given location impact daily life in both mundane (e.g., clothing choice, impacts to recreational activities) and societally disruptive (e.g., transportation delays, accidents due to hazardous conditions) ways. Accurately forecasting and monitoring transitions in precipitation type is also an extremely important, yet challenging, task. For instance, extreme cold season weather events such as United States East Coast "Nor'easter" storms typically have distinct rain–snow transition zones that separate warm and cold storm sectors [1–4]. The rain–snow line in such storms demarcates locations that receive potentially copious

amounts of snow versus rain accumulations. Similar surface precipitation phase-related complications arise in the United States East Coast and Midwest during cold air damming events that produce an array of precipitation types, including debilitating freezing rain, and frequent phase transitions that are intimately linked to near-surface thermodynamic composition [5]. Short-term surface precipitation phase monitoring is also important for flooding events that are exacerbated by rain falling on existing snowpack [6–9], while long-term surface rain versus snow observations are crucial for understanding climate-scale snowline trends in mountainous regions [10,11].

Remote sensing instruments are vital hydrologic monitoring tools and provide valuable global precipitation datasets, yet accurately classifying surface precipitation type solely through remote sensing observations is rife with complications, particularly for spaceborne instruments. Radar observations provide valuable information about surface precipitation type by identifying "bright bands" (abrupt, high values of reflectivity) aloft that indicate melting zones and likely surface rain [12], and/or dual-polarization signals that distinguish liquid versus solid hydrometeors [13,14]. Radar precipitation phase detection capabilities are diminished by blind zone complications in both spaceborne (e.g., first few clutter-affect range gates) and ground-based scanning (e.g., radar beam height located too high above the surface at long ranges) radar observations, especially when melting layers are located very close to the surface [15–17]. Spaceborne passive microwave sensors also provide precipitation estimates, but are sensitive to column-averaged properties and cannot easily distinguish surface precipitation phase. Therefore, passive microwave algorithms of precipitation commonly rely on model-derived thermodynamic fields to characterize the atmospheric profile and provide surface precipitation phase guidance [18]. Parameterizations have been developed that statistically determine surface phase type using key thermodynamic variables and thresholds, such as two meter and/or wet bulb temperature and thermodynamic lapse rates, which are determined from aggregated surface observer datasets [19–21].

Automated instruments can obtain precipitation information without the need for human intervention. Weighing gauges and tipping buckets are precipitation sensors that provide rate and accumulation measurements on varying time scales, but do not provide explicit phase identification [22]. The Automated Service Observing System (ASOS) network contains over 900 sensors deployed throughout the United States that provide precipitation rate (tipping bucket), precipitation identification (light emitting diode), and freezing rain identification (magnetostriction) capabilities. However, the ASOS observational suites provide no microphysical information, and tipping buckets may not effectively measure solid precipitation [23]. The Particle Size Velocity (Parsivel) laser-optical disdrometer and present weather sensor obtains precipitation phase information [24,25] and provides physically reasonable rainfall rates and raindrop size distributions [26,27], but struggles to resolve larger raindrops associated with intense rainfall rates [28] and snow microphysical properties [29].

This study describes the Precipitation Imaging Package PIP; [30,31], an in situ precipitation imager that skillfully discerns precipitation phase and provides robust microphysical information (e.g., particle size distribution, particle fall speeds, particle effective density, and precipitation rates) at high temporal sampling rates under solid, liquid, and mixed surface precipitation conditions. The PIP, along with a precipitation profiling radar, were deployed in the northern Great Lakes region at the Marquette, Michigan (MQT), National Weather Service (NWS) office in 2014 [32,33]. This enhanced observational suite focuses on cold season precipitation observations with direct applications to improving remote sensing quantitative precipitation retrievals, including surface precipitation rate and phase. The unique observing capabilities for surface precipitation are highlighted, including the ability of the PIP to properly characterize hydrometeor phase and provide reasonable precipitation accumulations under complicated mixed-phase and transitional events.

2. Data and Methods

2.1. Location

This study leverages observations from the MQT NWS office from January 2014 through the present [32,33]. This observational dataset consists of coincident remotely sensed and in situ observations of precipitation. Additionally, observations from co-located NWS instrumentation, surface measurements, and weather forecaster records are utilized. This region receives approximately 91 cm of rainfall and 200–500 cm of snowfall per year (geometric accumulation) per NWS observer records.

2.2. Instrumentation

2.2.1. Precipitation Imaging Package

The Precipitation Imaging Package (PIP) is a NASA-developed video disdrometer [30,31]. The PIP plays a major role in NASA Global Precipitation Measurement (GPM) mission ground validation (GV) campaigns as an inexpensive and easily deployable instrument [34]. The PIP consists of a high-speed video camera (380 frames per s) aimed at a bright halogen lamp at 2 m distance. The PIP has a field of view of 64 by 48 mm and image resolution of 0.1 by 0.1 mm. The PIP camera records videos of hydrometeors as they fall through the observation volume and produces hydrometeor characteristics, such as the particle equivalent area diameter and vertical and horizontal velocities. Higher order products from the PIP include particle size distributions (PSDs) and fall speed distributions at a 1 min resolution. The development of an empirically derived particle size, fall speed, and effective density parameterization [31] allows for retrievals of precipitation rates and precipitation phase discrimination capabilities [32,33,35]. The phase discrimination methodology is further described in Section 2.4.

2.2.2. Micro Rain Radar

The METEK Micro Rain Radar 2 (MRR) is a vertically profiling, 24-GHz frequency-modulated, continuous-wave Doppler radar [36]. The MRR has been used in field campaigns for observations of rain (e.g., [37]) and snow (e.g., [32,33,38,39]). The MRR at the MQT site is configured to profile the atmosphere to 3000 m above ground level (AGL) with a vertical resolution of 100 m and temporal resolution of 1 min.

2.2.3. Weather Radar

The NWS MQT office has an S-band Weather Surveillance Radar-1988 (WSR-88D), which is part of the Next Generation Weather Radar (NEXRAD) network. Level II data products for the NEXRAD system are available through the National Oceanic and Atmospheric Administration (NOAA) National Center for Environmental Information (NCEI) archive. In this work, we use WSR-88D observations of reflectivity, differential reflectivity, and cross correlation ratio from scans at 1.5° elevation angle.

2.2.4. Parsivel

An OTT Hydromet Particle Size Velocity 2 (Parsivel) laser disdrometer was added to the NWS MQT site in February 2017. The Parsivel is a laser-optical disdrometer that measures the diameter and fall speeds of hydrometeors. The Parsivel also produces hydrometeor phase identification for each particle [24]. The Parsivel identifies hydrometeor phase using the determined volume equivalent diameter and the fall speed of the particles. The Parsivel has been used successfully to examine the characteristics and precipitation rates of rain [26,27], while it is more limited in observing snowfall [29]. For this work, we are only using the Parsivel hydrometeor identification capabilities and we are limiting these to only identification of "rain" or "snow" (we are omitting the "mixed-phase", "rimed", and "ice pellet" categories).

2.2.5. Surface Meteorological Measurements

The surface meteorological data are obtained from the automated Davis Vantage Pro2 weather station, which is mounted on a tower (10 m AGL) adjacent to the NWS MQT office. Observations of surface temperature, dew point, and wind speed are recorded at one-minute intervals. The surface meteorological data are used to calculate the wet bulb temperatures in combination with an empirically derived formula from Stull et al. [40]. Precipitation observations are obtained five times per day by NWS MQT meteorologists at 0000, 0459, 0600, 1200, and 1800 UTC during ongoing precipitation events. Measurements of rain accumulation are collected using a 20.32 cm diameter standard rain gauge. Measurements of geometric snow accumulation are collected using a plastic, white snow board that is placed adjacent to the open snow stake field and cleared off between each measurement. Liquid water equivalent (LWE) measurements of snow are obtained from the melted snow in the rain gauge.

2.2.6. Weather Forecaster Records

The weather forecasters at the NWS MQT office keep daily records of precipitation. The 6-h accumulation is recorded for both rain and snow (geometric and LWE) at 0000, 0600, 1200, and 1800 UTC. In addition, start and stop times for observed precipitation type (e.g., rain showers, snowfall, fog) are recorded when these transitions occur (these are not restricted only to the 6-h observations). These records are archived and distributed by the NWS MQT office.

2.3. Reanalysis Products

This work utilizes the ERA5 reanalysis dataset [41] to examine the spatial surface values of mean sea level pressure (MSLP) and winds, and the 850 hPa pressure level temperature and winds in the region surrounding the NWS MQT. ERA5 temperature and relative humidity profiles are examined at specific time steps during precipitation phase transitions. Note that the ERA5 relative humidity is calculated by interpolating between the ice and water values using a quadratic function. The ERA5 products are available hourly from 1979 through 2020 and have a horizontal resolution of 31 km (globally) and 137 vertical layers to 0.01 hPa. This work uses reanalysis data in the region of 100° W to 70° W and 35° N to 55° N, and the grid point closest to the site (46.58° N, 87.58° W) for the profiles. The ERA5 profiles of temperature and relative humidity were used to calculate near surface lapse rates where pressure coordinates were converted to height coordinates using hydrostatic balance.

2.4. PIP Method for Determining Preipitation Phase

The PIP instrument uses observations of particle size and fall speed distributions in conjunction with an empirically derived parameterization to produce estimates of the bulk density of precipitation at 1 min resolution. This bulk effective density, hereafter $\overline{\rho_e}$, is described in detail in Pettersen et al. [31]. The relationship of $\overline{\rho_e}$ is shown in Equation (1):

$$\overline{\rho_e} = \frac{\frac{\pi}{6} \int \rho_e(D_e, V(D_e)) D_e^3 N(D_e) dD_e}{\frac{\pi}{6} \int D_e^3 N(D_e) dD_e} \tag{1}$$

where D_e is the particle equivalent diameter (i.e., the diameter of a spherical particle with the same projected area as that of the observed particle), $V(D_e)$ is the fall speed distribution, and $N(D_e)$ is the size distribution. A single $\overline{\rho_e}$ value represents the mean density of all the precipitation particles that fall during the 1 min period. The units of $\overline{\rho_e}$ are $g\,cm^{-3}$ and range from 0.015 to 1 (the density of liquid water). The parameterization produces maximum $\overline{\rho_e}$ values for particles with fallspeeds reaching those for raindrops as defined by Atlas and Ulbrich [42]. Further details on the $\overline{\rho_e}$ parameterization are found in Pettersen et al. [31].

Comparisons of PIP-observed particle fall speeds to the terminal velocity limits from Atlas and Ulbrich [42] are shown in Figure 1 for a rain-to-snow transition event from

24 to 25 October 2017. At 1100 UTC on 24 October 2017 (Figure 1a), the precipitation is rain phase only and the mean observed fall speeds as a function of D_e are roughly along the theoretical terminal velocity of rain. At 1730 UTC (Figure 1b) the fall speeds for the smaller particles ($D_e < 1$ mm) are along the theoretical terminal velocity of rain, while larger particles ($D_e > 1$ mm) have lower mean observed fall speeds than the theory predicts for rain. The PIP observations of precipitation at this time indicate a mix of rain and snow. At 2230 UTC on 24 October 2017, the PIP-observed mean fall speeds for particles at all sizes (D_e) are much lower than what is predicted from the terminal velocity of rain theory (Figure 1c), therefore designating that this event fully transitioned to snowfall.
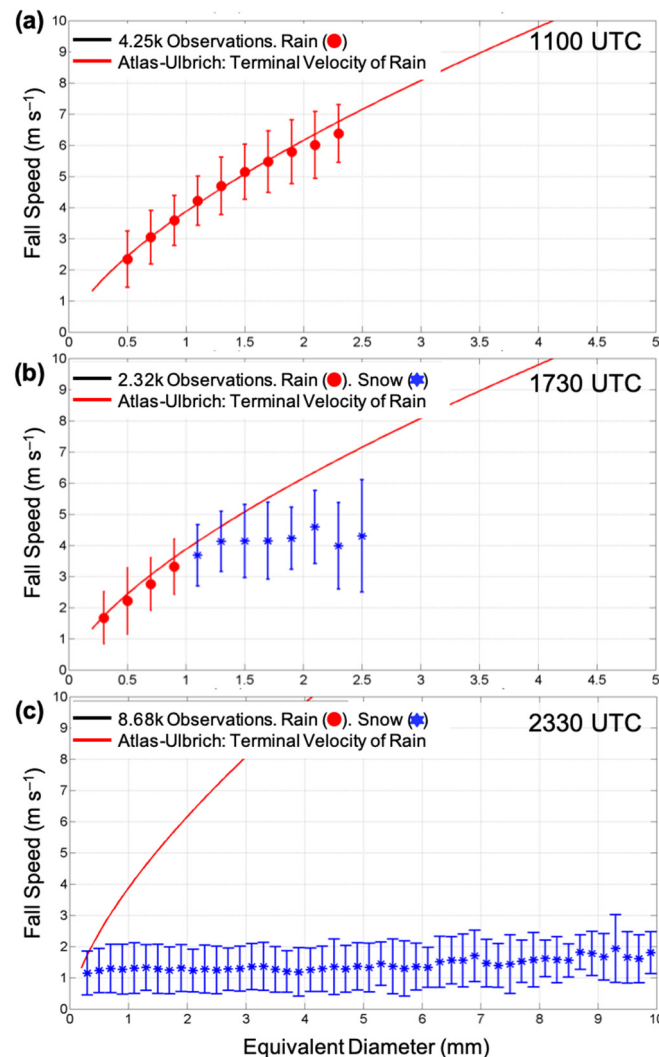

Figure 1. PIP observations of mean fall speed as a function of D_e for the example transition event on 24 October 2017. At 1100 UTC (**a**) all the precipitation is classified as rain (red circles) and particle fall speed is along the theorized terminal velocity of rain [42]. At 1730 UTC (**b**) a mixture of rain and snow exists (blue stars), as the larger particles have slower mean fall speeds (and depart from the theorized terminal velocity [42]). Finally, at 2330 UTC (**c**) only snow is present, as the mean fall speeds are much slower that the Atlas–Ulbrich terminal velocity for all D_e.

The example transitional event in Figure 1 demonstrates that observed precipitation microphysical characteristics can be used to elucidate precipitation phase. The $\overline{\rho_e}$ parameterization uses both fall speed and D_e and can therefore distinguish liquid and solid particles. In addition to bulk values of $\overline{\rho_e}$, the PIP also produces an effective density distribution as a function of particle size. The PIP PSDs and effective density distribution as a

function of D_e for the 24 to 25 October 2017 transition event are shown in Figure 2 (panels a and b, respectively). The PSD broadens as the precipitation transitions from predominately rain to mixed-phase (~1600 UTC) to snow (~2300 UTC). Through examination of events at the NWS MQT site and in Wallops, Virginia, an empirically derived effective density value of ≥ 0.85 g cm^{-3} indicates rain, while values <0.85 g cm^{-3} are classified as "non-rain". Non-rain can mean either mixed-phase precipitation or snowfall. This threshold was determined through examination of multiple independent events with co-located complementary instrumentation for assessing precipitation phase. The 0.85 g cm^{-3} threshold also accounts for the one standard deviation spread that is observed for the rain particle fall speeds, particularly at the larger diameters (e.g., Figure 1a).
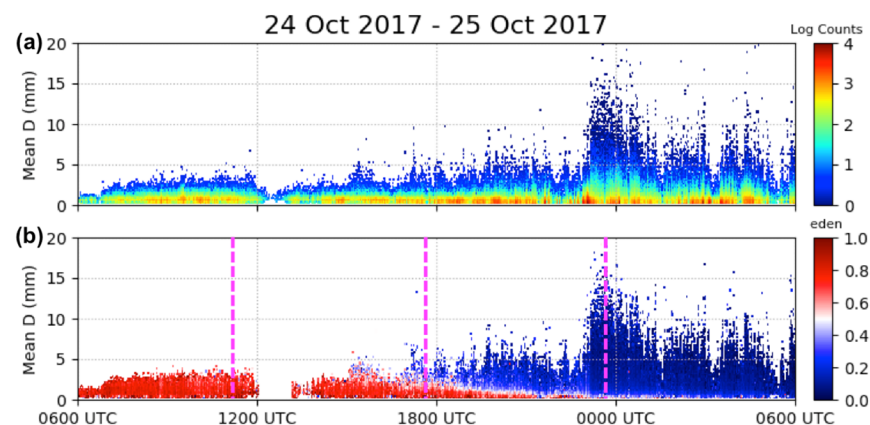

Figure 2. PIP observations during an event from 24 October 2017 at 0600 UTC to 25 October 2017 at 0600 UTC. The top panel (**a**) illustrates the PIP DSD values and the bottom panel (**b**) shows the PIP determined effective density. The dashed magenta lines highlight 1100, 1730, and 2330 UTC, which are the times used to highlight precipitation characteristics in Figure 1.

At the NWS MQT site, we find that snowfall tends to have effective density values between 0.015 and 0.25 g cm^{-3}. Mixed-phase precipitation effective density is >0.25 g cm^{-3} and <0.85 g cm^{-3}, but is rarely observed compared to rain and snow. The range of values observed during snowfall events, as confirmed by the NWS MQT office and ancillary observations is consistent with previous in situ studies of ice and snow particles from aircraft probes [43]. Note that the PIP cannot currently verify the presence/absence of riming. Rimed particles will increase the mass and therefore the fall speed of the particles and may contribute to the uncertainty of the partitioning method (see Pettersen et al. [31] for details).

3. Results

We identified 13 independent events at the NWS MQT site between 1 January 2017 and 1 January 2020 with at least one precipitation phase transition. These events include observations of coincident PIP, MRR, WSR-88D, Parsivel, surface meteorological observations, and weather forecaster records. We first assess the precipitation phase transition times determined by the PIP and compare to the NWS MQT weather forecaster records. We also compare the PIP-produced LWE accumulation to the NWS MQT measurements. Finally, we examine in depth four precipitation events: two rain-to-snow transition events, a multiple transition event, and a prolonged mixed-phased event.

3.1. Phase Transition Event Timelines and Characteristics

Table 1 outlines the observations from the PIP and the NWS MQT forecaster records for 11 events with a single precipitation phase transition. We found that rain-to-snow precipitation phase transition events are more common than snow-to-rain events during the 2017 to 2020 seasons. Three of the events transition from snowfall to rain, while eight

events transition from rain to snowfall. All events examined were required to be a minimum of 6-h duration and range from 7 to 20 h.

Table 1. Events with a single precipitation phase transition with observations from the PIP and the NWS MQT forecaster records. * Denotes +1 day UTC from start date.

Event Date	Precip. Phase	PIP Times	NWS Times	Precip. Phase	PIP Times	NWS Times
10 February 2017	Snow	1035 UTC 1700 UTC	1045 UTC 1715 UTC	Rain	1648 UTC 1833 UTC	1645 UTC 1830 UTC
23 February 2017	Rain	0300 UTC 0425 UTC	0300 UTC 0430 UTC	Snow	0425 UTC 1108 UTC	0430 UTC 1115 UTC
27 April 2017	Rain	0745 UTC 1755 UTC	0750 UTC 1750 UTC	Snow	1753 UTC 2350 UTC	1750 UTC 2345 UTC
24 October 2017	Rain	0550 UTC 2130 UTC	0600 UTC 2000 UTC	Snow/Mixed	1515 UTC 0720 * UTC	1525 UTC 0730 * UTC
2 November 2017	Snow	0325 UTC 0820 UTC	0250 UTC 0845 UTC	Rain	0723 UTC 1035 UTC	0730 UTC 1055 UTC
5 December 2017	Rain	0250 UTC 0945 UTC	0235 UTC 0950 UTC	Snow	1000 UTC 1230 UTC	1015 UTC 1215 UTC
11 January 2018	Rain	1440 UTC 1655 UTC	1445 UTC 1645 UTC	Snow	1630 UTC 0000 * UTC	1625 UTC 0000 * UTC
7 November 2018	Rain	0035 UTC 0835 UTC	0050 UTC 0835 UTC	Snow	0615 UTC 2125 UTC	0635 UTC 2110 UTC
11 April 2019	Snow	1945 UTC 0255 * UTC	1945 UTC 0300 UTC	Rain/Mixed	1930 UTC 0820 * UTC	1945 UTC 0815 * UTC
21 November 2019	Rain	0940 UTC 1700 UTC	0940 UTC 1650 UTC	Snow	1650 UTC 0000 * UTC	1650 UTC 0000 * UTC
30 December 2019	Rain	0855 UTC 1120 UTC	0900 UTC 1110 UTC	Snow	1105 UTC 2100 UTC	1110 UTC 2100 UTC

For the snow-to-rain transition events, the observed onsets of snowfall from the PIP and the NWS MQT are within 15 min, and the identified ends of the snowfall are within 25 min. The onsets of the rain in the second periods of the events are within 15 min, and the ends of the rain are within 20 min, as observed by the PIP and NWS MQT.

For the eight rain-to-snow transition events, we see similar agreement between the observing methods. The PIP and NWS MQT observed that the onsets of the rain are within 15 min of each other and within 10 min for observed ends, with the exception of 24 October 2017 where the end times differed by 90 min. The second part of the rain-to-snow transition events had the onsets of snowfall within 20 min and the ending of snowfall within 15 min between the PIP and NWS MQT observations. The 24 October 2017 event had an unusually long transition between rain to snowfall and much of the precipitation between 1800 and 2200 UTC was identified as mixed by the PIP instrument (Figure 2b). Events with prolonged periods of mixed-phase precipitation are harder to characterize for the PIP and are potentially more subjective for the NWS forecaster, so there will be more inherit variability in classifying these cases and they will be more likely to exhibit differences between observing methods.

Table 2 outlines the observations from the PIP and the NWS MQT forecaster records for the two events with multiple precipitation phase transitions. Both of these events started as snowfall, transitioned to rain, and then transitioned back to snowfall. The event beginning on 17 November 2017 was 15 h duration and the event beginning on 27 December 2018 was 30 h duration. The onsets of the first snowfall period for both events agreed within 10 min between the PIP and NWS MQT observations, and the endings within 20 min. The respective onsets of rain for the 17 November 2017 event were within 15 min, but a much larger 65 min difference in rain onsets was reported for the 27 December 2018 event. The endings of the rain periods were within 15 min between the PIP and NWS MQT observations. The onsets of the second snowfall period for both events were within 10 min and the observed endings within 5 min between the observations.

Table 2. Events with a multiple precipitation phase transitions with observations from the PIP and the NWS MQT forecaster records. * Denotes +1 day and ** denotes +2 UTC from start date.

Event Date	Precip. Phase	PIP Times	NWS Times	Precip. Phase	PIP Times	NWS Times	Precip. Phase	PIP Times	NWS Times
17 November 2017	Snow	1255 UTC 1450 UTC	1300 UTC 1435 UTC	Rain	1645 UTC 2345 UTC	1630 UTC 2350 UTC	Snow	2345 UTC 0300 * UTC	2350 UTC 0300 * UTC
27 December 2018	Snow	0930 UTC 1855 UTC	0925 UTC 1910 UTC	Rain	1955 UTC 1030 * UTC	2100 UTC 1015 * UTC	Snow	1005 * UTC 0125 ** UTC	1015 * UTC 0130 ** UTC

In addition to examining observed precipitation onset and termination and phase, we compare the measured accumulation between the PIP and the NWS MQT methods. Accumulations (in LWE) for the events are shown in Table 3, as well as differences in PIP accumulations relative to the NWS measurements and wind speeds. The PIP and NWS MQT estimates of accumulation are within 10% for 11 of the 12 of the events. The 24 October 2017 event had a much larger difference with the PIP underestimating the accumulation relative to the NWS MQT by 34.3%. Notably, this event had an unusually prolonged period (>6 h) of mixed phase precipitation (identified by both of the PIP and the NWS MQT). In addition, this event experienced the highest mean and maximum wind speeds of all the events examined, which would impact accurate retrieval of precipitation totals from both methods, particularly during the snowfall. Interestingly, the two events with multiple transitions (17 November 2017 and 27 December 2018) displayed mostly consistent measurements, with differences of only 7.7% and 2.7%, respectively.

Table 3. Accumulations in LWE from the PIP and NWS observations and percentage difference for all the precipitation transition events. Differences are calculated by subtracting the NWS from the PIP accumulation and then dividing by the PIP accumulation. Mean and maximum wind speeds during the events are included. * Denotes +1 day and ** denotes +2 UTC from start date.

Event Date	PIP LWE (mm)	NWS LWE (mm)	Diff. % PIP–NWS	Mean WS (m s^{-1})	Max WS (m s^{-1})
10 February 2017 1000–1800 UTC	2.32	2.54	−9.4	3.94	5.81
23 February 2017 0200–1200 UTC	11.01	10.16	7.7	3.57	5.36
27 April 2017 0800–0000 * UTC	17.58	17.78	−1.1	0.33	0.83
24 October 2017 0600–0800 * UTC	39.71	53.34	−34.3	6.78	12.07
2 November 2017 0300–1200 UTC	3.23	3.55	−9.9	1.33	2.68
17 November 2017 1200–0600 * UTC	8.53	7.87	7.7	2.66	5.36
5 December 2017 0200–1200 UTC	4.74	4.57	3.6	6.05	11.17
11 January 2018 1400–0000 * UTC	9.90	9.65	2.5	2.76	6.23
7 November 2018 1000–0000 ** UTC	3.74	3.56	4.8	3.62	5.81
27 December 2018 0000–0000 ** UTC	16.97	16.51	2.7	3.41	6.71
11 April 2019 1800–1200 * UTC	34.59	32.26	6.7	3.29	6.71
21 November 2019 1000–0000 * UTC	9.31	10.16	−9.1	3.29	6.23
30 December 2019 0800–2100 UTC	24.03	23.11	3.8	2.32	4.02

3.2. Detailed Observations of Example Cases

Here we present detailed observations of four cases: two rain-to-snow transition events (11 January 2018 and 21 November 2019), one multiple precipitation phase transition

event (27 December 2018), and a prolonged mixed-phase precipitation event (24 October 2017). We focus on highlighting the ability of the PIP to accurately identify the precipitation phase during these complex events and use ancillary data from the MRR, Parsivel, surface observations, WSR-88D, and ERA5 reanalysis data products to support the PIP phase identification.

3.2.1. Rain-to-Snow Transition Events

The first event examined in detail is a rain-to-snow transition event on 11 January 2018 lasting a total of nine hours. High-temporal resolution profile and surface observations for this event are shown in Figure 3. The PIP and NWS MQT office identified rain beginning at approximately 1445 UTC and snow beginning at approximately 1630 UTC (Table 1). The precipitation transition is seen in the PIP estimates of density in Figure 3d where the red (rain) transitions to mostly blue (snow). Additionally, the PIP observes generally small particles and narrow PSDs during the rain period, whereas after the transition to snowfall the PIP PSDs are much broader with larger particles. The PIP and the Parsivel (Figure 3d, dots) also show a similar rain to snowfall transition near 1630 UTC.
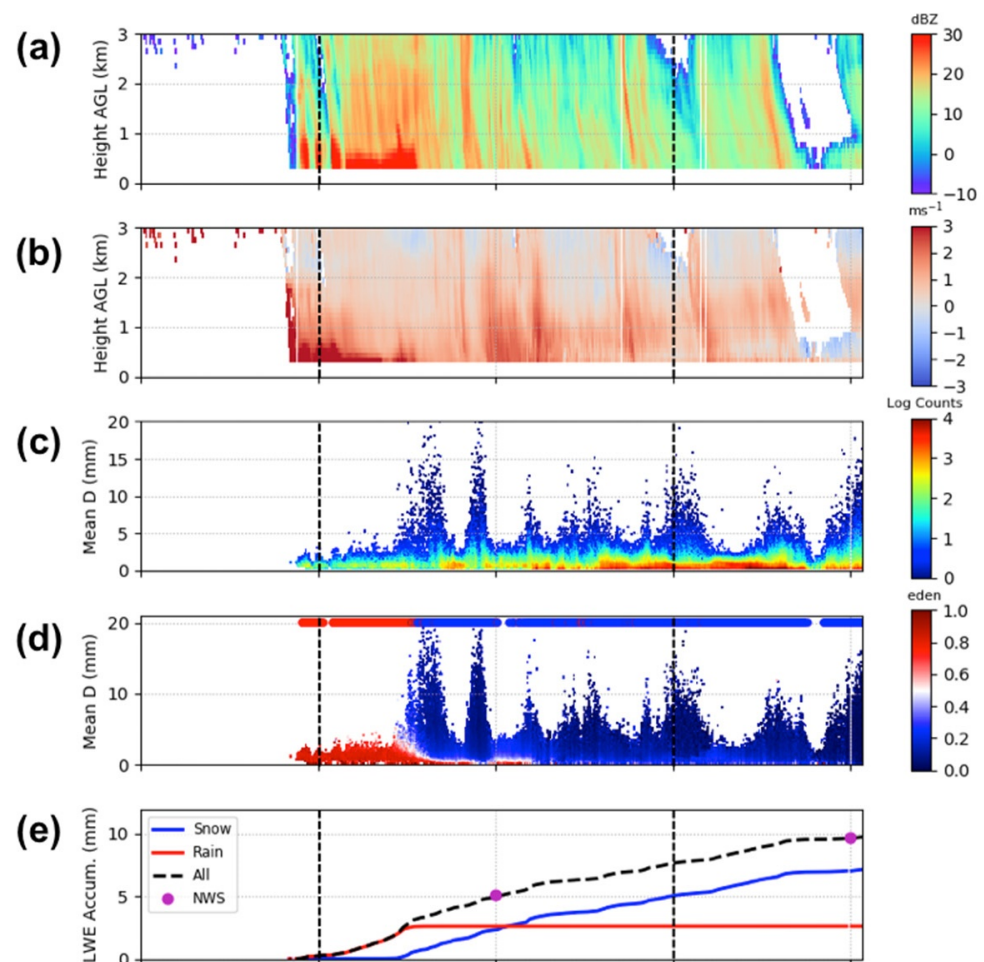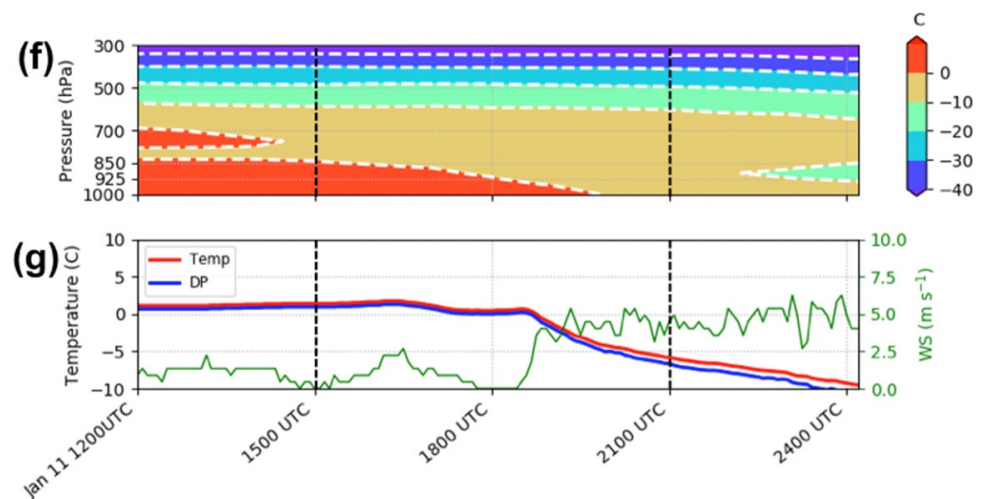

Figure 3. *Cont.*

Figure 3. Observations during the 11 January 2018 rain-to-snow transition event. Shown are MRR reflectivity (**a**) and Doppler velocity (**b**), PIP PSDs (**c**) and density estimates (**d**), Parsivel hydrometeor identification (d, red and blue dots on the upper portion of the panel), PIP and NWS LWE accumulation (**e**), ERA temperature profiles (red >0 °C) (**f**), and surface temperature, dew point, and winds (**g**). The dashed lines indicate time periods examined in the next figure.

There is also evidence of the precipitation phase transition in the MRR profile observations. Enhanced values of reflectivity (>25 dBZ) exist in the lowest 800–1000 m above ground level (AGL) at the onset of the rain at ~1445 UTC to the transition to snowfall at 1630 UTC, when the enhanced low-level reflectivity values abruptly end (Figure 3a). Additionally, the profiles of MRR Doppler velocities are much larger near the surface during the rain period of the event than during the snow period, indicating higher particle fall speeds consistent with the PIP-classified rain phase. The profiles of temperature from the ERA5 reanalysis denote a deep layer of temperatures >0 °C extending to ~850 hPa (top of the boundary layer) until about 1700 UTC. Afterwards, the relatively warm air diminishes and colder air (<0 °C) moves into the lower levels of the atmosphere (Figure 3f). Again, the progression of the profile temperatures is consistent with the timing of the transition of rain to snowfall identified by PIP observations.

The precipitation accumulation estimates from the PIP agree well with the 6-h observations from the NWS MQT both during the rain-dominated and snow-dominated periods (Figure 3e), with about 3 mm rain and ~7.5 mm snow (LWE). The surface temperatures are around +1 °C from the onset of the precipitation to ~1630 UTC where they dip slightly to just above freezing (Figure 3g). The temperature drops rapidly below freezing at approximately 1900 UTC, well after the observed onset of the snowfall. The wind speeds also increase at 1900 UTC. The trend of the surface temperatures throughout the event is consistent with rain transitioning to snowfall.

Examining the spatial distribution of the ERA5 surface mean sea level pressure (MSLP) and winds (Figure 4a,b) and the 850 hPa temperature and winds (Figure 4c,d) helps illuminate the synoptic conditions occurring during the rain and snow periods of this event. At 1500 UTC, during the rain period of the event, a front is moving through the region with low pressure and calm surface winds located at the NWS MQT site (Figure 4a). The 850 hPa temperatures are above freezing at this time with light winds out of the southwest (Figure 4c). At 2100 UTC, during the snowfall period of the event, the low pressure moved east of the NWS MQT site (Figure 4b) and the cold front arrived with 850 hPa temperature below freezing and a steep temperature gradient to the west of the site (Figure 4d). The synoptic conditions depict the movement of a cold front into the region, which is again consistent with the PIP observations showing rain transitioning to snowfall during the event.
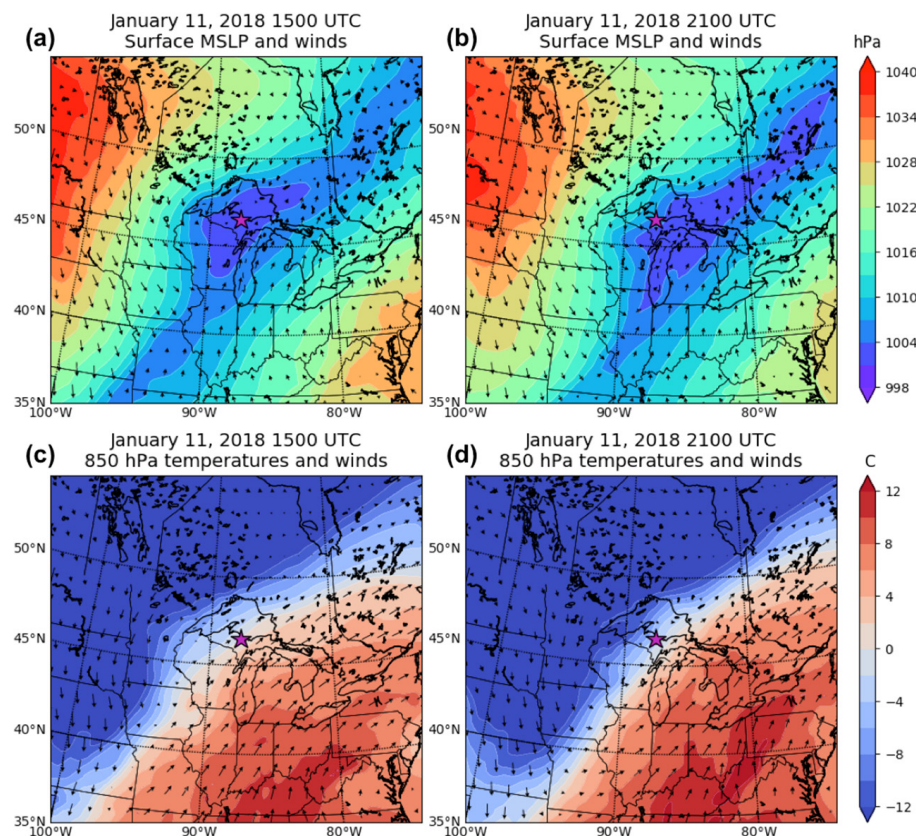
Figure 4. ERA5 MSLP and surface winds and 850 hPa temperatures and winds for 11 January 2018 at 1500 (**a**,**c**) and 2100 UTC (**b**,**d**). The purple star denotes the location of NWS MQT.

The second event also exhibits a transition from rain to snowfall, however with a longer period of rain and several key profile changes as the rain evolves before switching to snowfall. This rain-to-snow event occurred on 21 November 2019 and was approximately 14 h in duration (Figure 5). The PIP and the NWS MQT observed rain beginning at 0940 UTC and ending around 1650–1700 UTC, with snowfall onset at 1650 UTC. The precipitation transition is identified in the PIP estimates of density in Figure 5d where the red (rain) transitions to blue (snow). The PIP PSDs exhibit generally small particles and narrow width during the rain period, while after the transition to snow, the PIP PSDs are broader and contain larger particles. There is again very good agreement between the PIP and the Parsivel (Figure 5d, dots) for the precipitation phase transition at 1650 UTC.

Similar to the previous event, there are distinct melting layer and rain signatures in the MRR profile observations. There is evidence of a bright band and enhanced reflectivities (>25 dBZ) in the lowest ~2 km AGL from the onset of the rain to ~1300 UTC, at which point the layer of enhanced reflectivities becomes very shallow (<1 km) and continues to taper until disappearing entirely at 1650 UTC (Figure 5a). The profiles of MRR Doppler velocity show higher fall speeds in the same period as the enhanced reflectivities (Figure 5b), indicating that the precipitation is rain. This rain period coincides with the timing of rainfall indicated by the PIP. The profiles of temperature from the ERA5 reanalysis denote a much deeper layer of warm temperatures (>0 °C) extending to almost 700 hPa through 1400 UTC. The 0 °C isotherm then starts to slowly descend reaching 925 hPa at 1800 UTC (Figure 5f), after the onset of the snowfall, at which point the temperatures above the 925 hPa level are below freezing. The profile observations from the MRR and the ERA5 reanalysis are consistent with the observations and timing of the transition of rain to snowfall seen by the PIP.
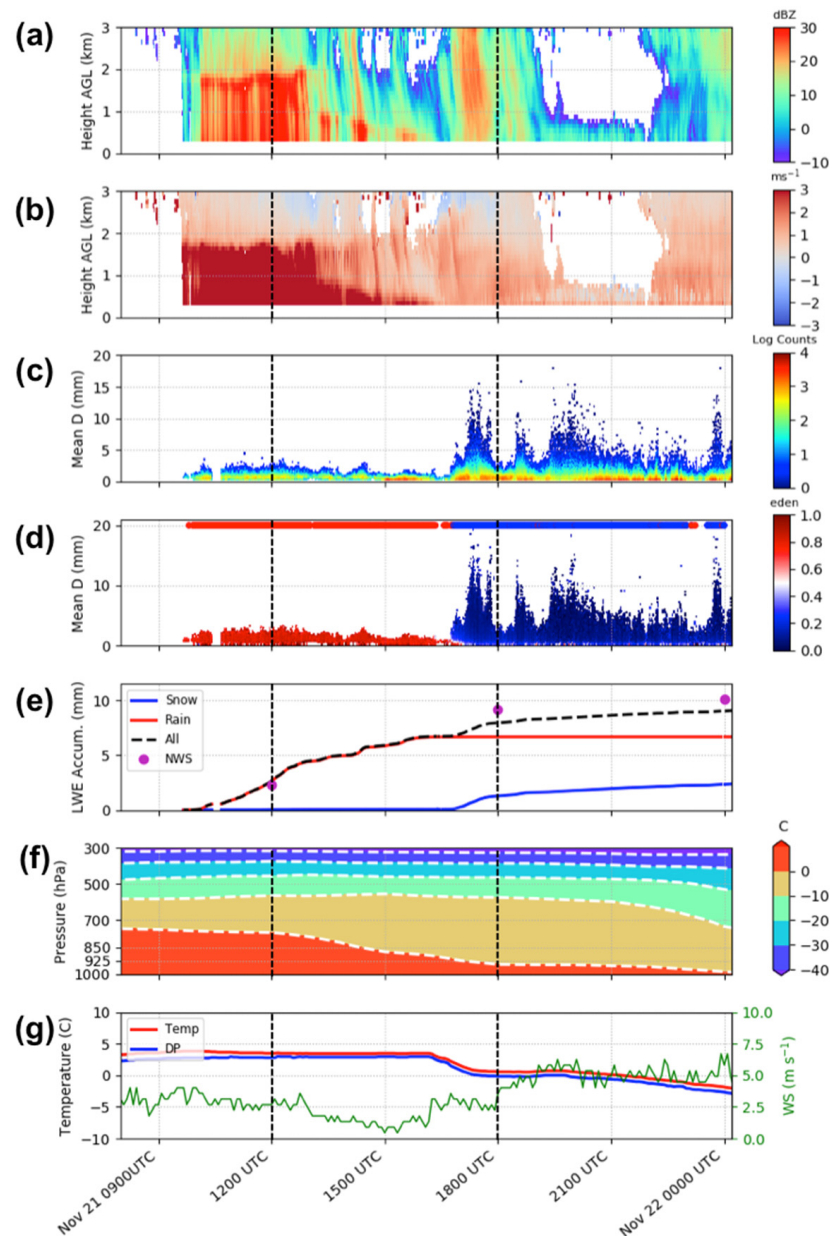
Figure 5. Observations during the 21 to 22 November 2019 event rain-to-snow transition event. Shown are MRR reflectivity (**a**) and Doppler velocity (**b**), PIP PSDs (**c**) and density estimates (**d**), Parsivel hydrometeor identification (**d**, red and blue dots on the upper portion of the panel), PIP and NWS LWE accumulation (**e**), ERA temperature profiles (red > 0 °C) (**f**), and surface temperature, dew point, and winds (**g**). The dashed lines indicate time periods examined in the next figure.

The surface observations of LWE accumulation from the PIP agree with the 6-h measurements from the NWS MQT, particularly during the rain-dominated periods (Figure 5e). The total accumulation in LWE was ~6.5 mm rain and 2 mm snow. The surface temperature is around +4 °C from the onset of the precipitation to ~1600 UTC, at which time it decreases, reaching 0 °C at 1650 UTC and stabilizing until 2100 UTC when it again slowly cools to below freezing (Figure 3g). It is notable that the snowfall starts while the surface temperatures are still several degrees above freezing. Wind speeds increase from 2.5 to 5 m s^{-1} at 1800 UTC. Again, the patterns of the surface observations throughout the event are consistent with rain transitioning to snowfall.

WSR-88D observations are also used to determine the precipitation phase during the transition events. The spatial patterns of reflectivity, differential reflectivity (Z_{DR}), and

cross correlation ratio (ρ_{HV}) can illuminate characteristics of the precipitation, as these observations contain information about hydrometeor type and can be used to identify the location of the melting level [44–46]. Figure 6 illustrates the spatial extent of the reflectivity, Z_{DR}, and ρ_{HV} during the rain period at 1203 UTC (a,b,c) and during the snowfall period at 1804 UTC (d,e,f). At 1203 UTC on 21 November 2019, the WSR-88D shows widespread reflectivities exceeding 25 dBZ in the NWS MQT region (Figure 6a). There are also larger values of Z_{DR} (Figure 6b) and relatively low values of ρ_{HV} (Figure 6c) in the northwest quadrant of the observational area. This region of higher reflectivity, larger Z_{DR}, and low ρ_{HV} values indicate that there is likely a mix of rain and ice/snow precipitation. This area is ~30 to 40 km from the WSR-88D and therefore this layer of mixed precipitation is between 0.75 and 1.05 km AGL (assuming standard atmospheric refraction). This height range is slightly higher than the MRR-indicated melting level (Figure 5a,b), but it does indicate that the surface precipitation phase is rain, which agrees with the PIP and other surface and profile observations at 1203 UTC. At 1804 UTC the WSR-88D reflectivities are more variable, with intensities ranging from 10 to 35 dBZ (Figure 6d). The values of Z_{DR} are generally small and ρ_{HV} generally high (Figure 6e,f, respectively), and there are no indications of melting or hydrometeor phase changes. The observations from the WSR-88D indicate that the precipitation at this time is snowfall, which is consistent with PIP observations.
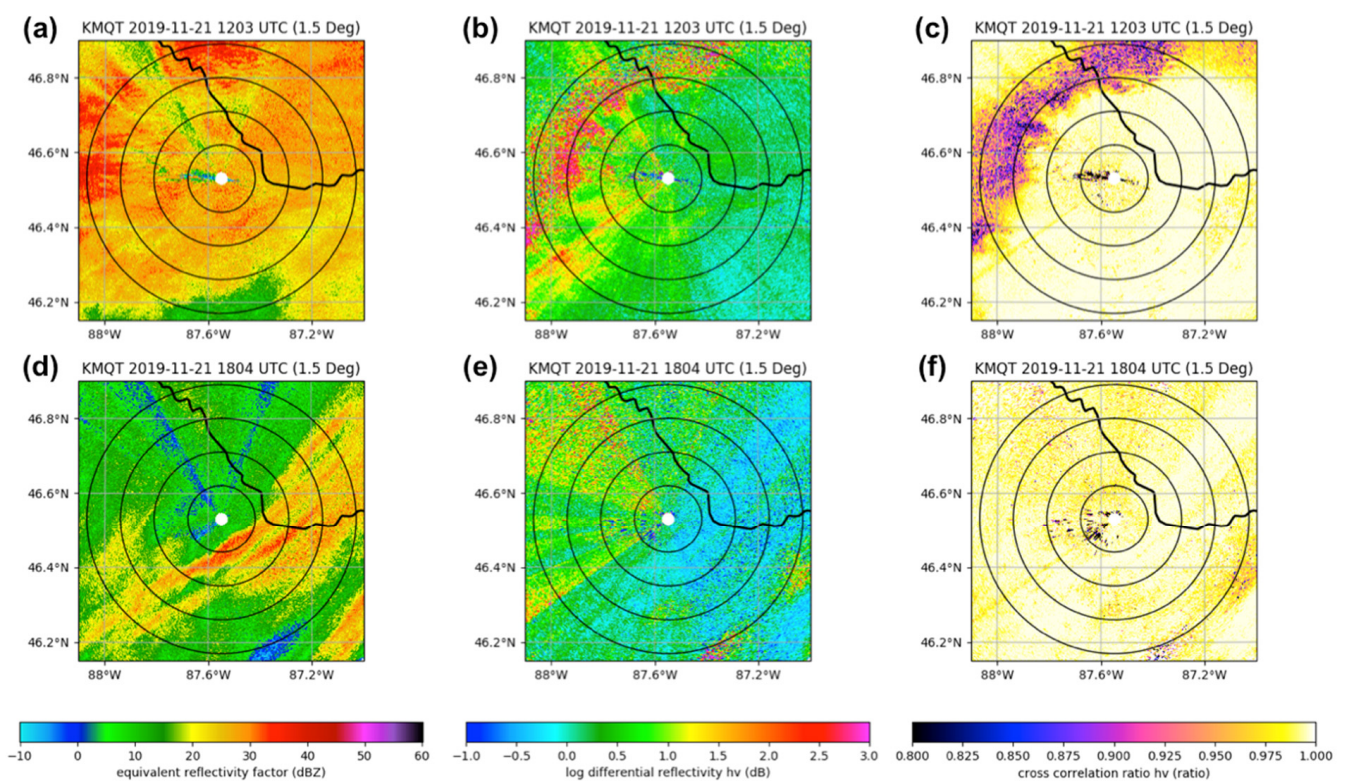

Figure 6. WSR-88D values of reflectivity, differential reflectivity (Z_{DR}), and cross correlation ratio (ρ_{HV}) during the rain period (1203 UTC, panels (**a–c**) and the snow period (1804 UTC, panels (**d–f**)) for the event on 21 November 2019. The rings denote 10 km radial distance from the radar.

3.2.2. Snow-to-Rain-to-Snow Transition Event

A multiple precipitation phase transition event is shown in Figure 7. This event lasted 30 h starting on 27 December 2018 at 0930 UTC and began as snowfall, then changed to rain at ~2000–2100 UTC for 13 h before transitioning back to snowfall at 1000 UTC on 28 December 2018. The multiple transitions are clearly discernable as the sections of blue (snow), red (rain), and blue (snow) in the PIP density estimates during the event (Figure 7d), and these transitions generally agree with the Parsivel observations (Figure 7d,

dots). However the Parsivel has missing data during the rain period, likely due to the sporadic and light nature of the precipitation during this time. The PIP PSDs (Figure 7c) are fairly broad with an abundance of small particles during the first snowfall period, with indications of even larger particles during the second snowfall period. During the rainfall period of this event the PIP PSDs are narrow and there are periodic gaps, providing more evidence of very light precipitation rates.
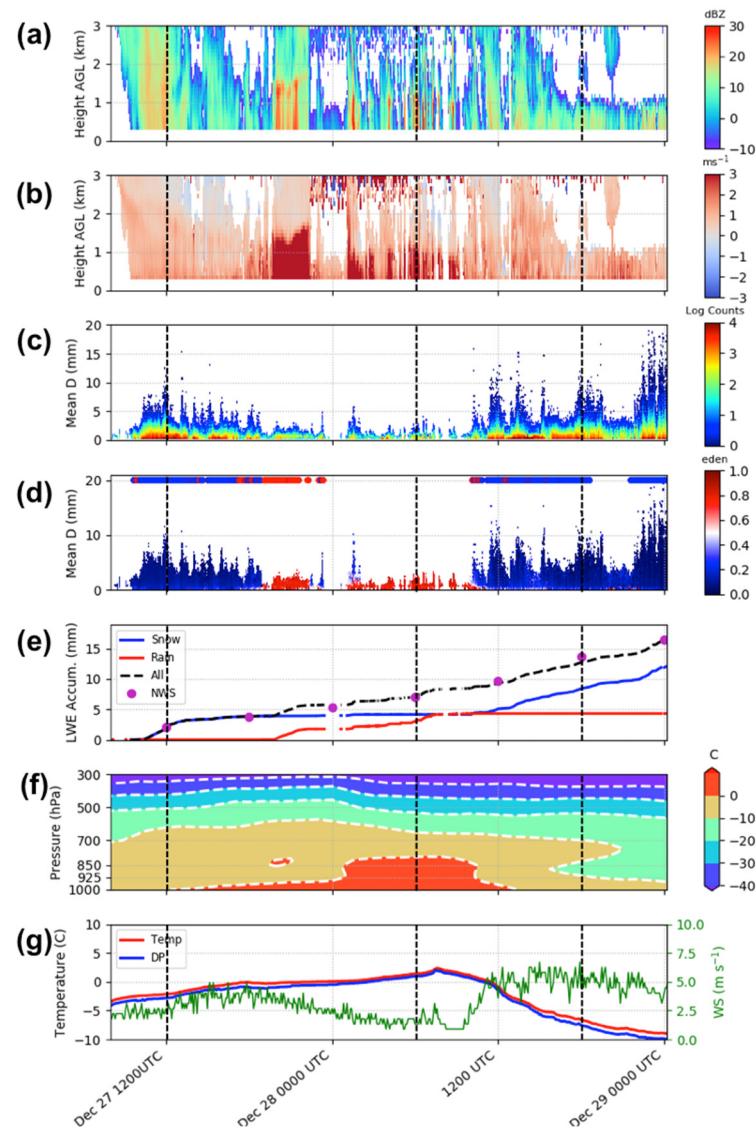

Figure 7. Observations during the 27 to 28 December 2018 event rain-to-snow transition event. Shown are MRR reflectivity (**a**) and Doppler velocity (**b**), PIP PSDs (**c**) and density estimates (**d**), Parsivel hydrometeor identification (d, red and blue dots on the upper portion of the panel), PIP and NWS LWE accumulation (**e**), ERA temperature profiles (red >0 °C) (**f**), and surface temperature, dew point, and winds (**g**). The dashed lines indicate time periods examined in the next figure.

The beginning of the precipitation event is dominated by a deep layer of falling snow, as seen by the MRR profiles of reflectivity and Doppler velocities (Figure 7a,b). Melting layers are clearly indicated in the MRR profile observations, as there is a noticeable bright band in the reflectivity and an abrupt increase in Doppler velocities beginning at ~2000 UTC 27 December (Figure 7a,b). The melt layer starts out at ~1.5 km AGL and is continuous, but becomes shallower (1 km AGL) and sporadic starting at ~0100 UTC on 28 December. There is some indication of a short period of mixed-phase precipitation, both

from the MRR and PIP, at 0000 UTC on 28 December. The second transition, starting at 1015 UTC on 28 December, is dominated by shallow, lake-effect snowfall with MRR echo top heights <1 km AGL (Figure 7a). The profiles of ERA5 reanalysis temperatures illustrate a shallow layer of >0 °C air starting at 1200 UTC and growing to a much deeper layer (up to 850 hPa) between 0000 and 1200 UTC on 28 December (Figure 7f), during which time the precipitation is generally rain, after which the profile cools considerably. The evolution of the profile temperatures is consistent with the timing of the transition of snowfall to rain to snowfall identified by PIP observations.

The LWE accumulation estimates between the PIP and the 6-h NWS MQT measurements are remarkably consistent throughout the entire 30 h event (Figure 7e). The total accumulation was ~17 mm LWE, with snowfall accounting for 12 mm (LWE) and rain the remaining 5 mm. The surface temperatures started out below freezing (-4 °C) and then slowly warmed to a maximum of $+2$ °C at ~0700 UTC on 28 December, when they then rapidly cooled to -10 °C (Figure 7g). The winds speeds are light (2.5 m s^{-1}) for the first snowfall and rain periods of the event, and abruptly increase as surface temperatures fell.

Profiles of temperature and relative humidity from the ERA5 reanalysis can be used to further understand the precipitation phase transitions. Figure 8a shows the temperature profiles for 27 December at 1200 UTC, and 28 December at 0600 and 1800 UTC. During the first snow period of the event, the near-surface temperatures are about 0 °C and slowly cool with height (solid line). During the rain period, the temperatures are above 0 °C until about 800 hPa (dashed line). In the second snow period of the event the temperatures are much colder (<-5 °C) and a pronounced inversion exists around 850 hPa (dotted line). The relative humidity profiles (Figure 8b) show larger values throughout the profile at the beginning of the event during the deep snowfall period (solid line), large values to ~750 hPa during the rain period (dashed line), and a drier, oscillating profile during the shallow, lake-effect snowfall period (dotted line). The profiles of the temperature and relative humidity for the deep and shallow (lake-effect) snowfall periods are consistent with previous studies at the NWS MQT site [32,33]. The progression of the temperature profiles is consistent with the PIP observations of snowfall transitioning to rain and then back to snowfall.
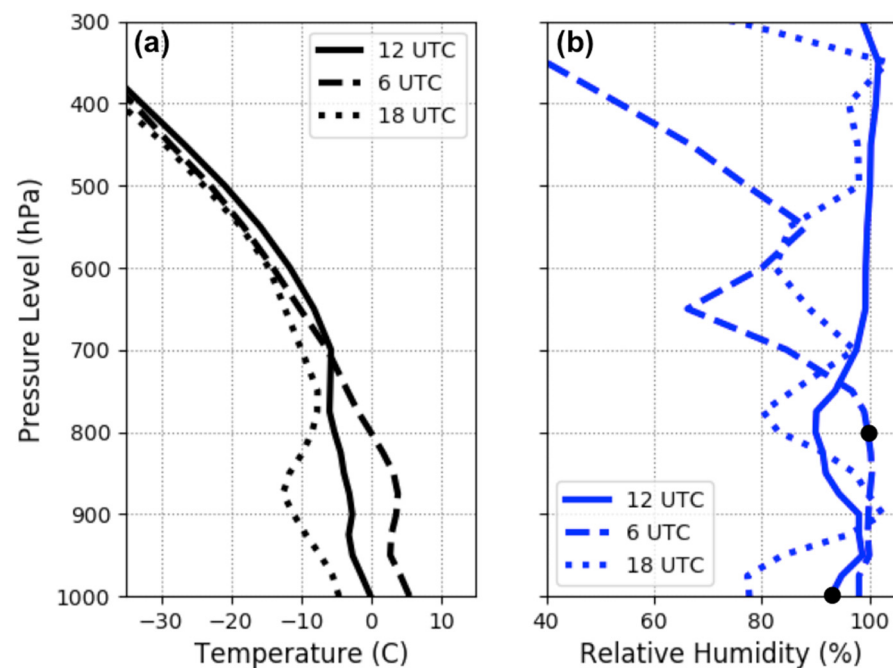

Figure 8. Profiles of temperature (**a**) and relative humidity (**b**) from the ERA5 reanalysis for 27 December 2018 at 1200 UTC (solid line), 28 December 2018 at 0600 UTC (dashed line) and 1800 UTC (dotted line). The black dots in panel b signify the 0 °C level for the 1200 and 0600 UTC profiles.

3.2.3. Mixed-Phase Precipitation Event

An event with a remarkably long period of mixed-phase precipitation is featured in Figure 9. This event lasted approximately 26 h starting on 24 October 2017 at 0550 UTC and ending on 25 October at 0730 UTC. There was a prolonged period of mixed-phase precipitation starting on 24 October at 1700 UTC and ending at 2300 UTC. During this period, the PIP indicated both rain (red) and snow (blue) precipitation, while the Parsivel toggled back and forth between rain and snow identification (Figure 9d, dots). The predominately rainfall period is between 0600 UTC and 1700 UTC, and the raindrops are noticeably large, with some >2 mm effective diameter (Figure 9c). Large snow particles (>10 mm) emerge at ~2200 UTC, as seen in both the PIP PSDs (Figure 9c) and the density distribution estimates (Figure 9d), particularly around 0000 UTC on 25 October.
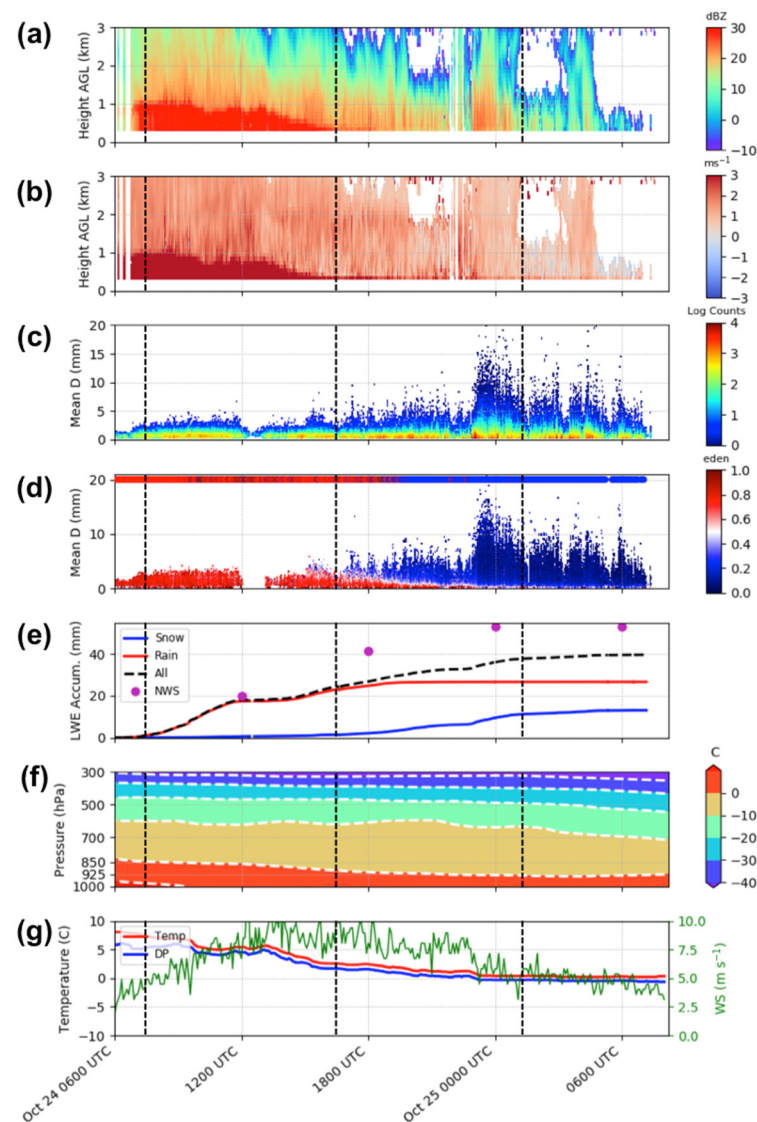
Figure 9. Observations during the 24 to 25 October 2017 event rain-to-snow transition event. Shown are MRR reflectivity (**a**) and Doppler velocity (**b**), PIP PSDs (**c**) and density estimates (**d**), Parsivel hydrometeor identification (d, red and blue dots on the upper portion of the panel), PIP and NWS LWE accumulation (**e**), ERA temperature profiles (red >0 °C) (**f**), and surface temperature, dew point, and winds (**g**). The dashed lines indicate time periods examined in the next figure.

Radar reflectivities and Doppler velocities increase appreciably in the lowest 1 km AGL at the beginning of the event, indicating the melting level of the precipitation (Figure 9a,b).

The melted layer persists until 1400 UTC when it starts to diminish. Higher Doppler velocities are also observed in the near-surface bin of the MRR profile until ~2200 UTC (Figure 9b), coinciding with most of the extended mixed-phase precipitation period, as indicated by both the PIP and Parsivel (Figure 9d). The profiles of ERA5 reanalysis temperatures illustrate a layer of >0 °C air up to 850 hPa at the onset of the precipitation, and the layer gradually becomes increasingly shallow throughout the event, descending to ~925 hPa (Figure 9f). Notably, the ERA5 reanalysis temperature profiles indicate that the surface temperatures were >0 °C for the entirety of the event. This agrees with the observed surface temperatures (Figure 9g), which were 8 °C at the beginning of the event and slowly cooled to 0 °C at ~2330 UTC and dropped to just below freezing (−1 °C) at 0300 UTC on 25 October. This very slow decline in temperatures and progressive cooling of the profile is consistent with the prolonged period of mixed-phase precipitation observed by the PIP.

The LWE accumulation estimates from the PIP and the 6-h NWS MQT measurements are consistent for the first part of the rain period of the event, between 0600 and 1200 UTC (Figure 9e). However, after 1200 UTC, these estimates diverge with the PIP LWE accumulation 34% lower than the NWS MQT measurements by the end of the event. Two significant features of this event differ from the others: (1) this event exhibits a period of 6-h period of mixed phase precipitation, and (2) the wind speeds are by far the highest of all the events examined. The PIP uses an empirically determined parameterization to estimate the densities of particle and glean precipitation rates, which does not have observations from mixed-phase or high snow density events (see details in Pettersen et al. [31]). The lack of parameterization constraints may impact retrievals of mixed-phase precipitation. Additionally, the wind speeds increase to >10 m s^{-1} at 1200 UTC on 24 October (Figure 9g), which impact the accumulation measurements from both the PIP and the NWS MQT snow board and precipitation gauges.

Investigation of the spatial distribution of the ERA5 reanalysis surface MSLP and winds (Figure 10a–c) and the 850 hPa temperature and winds (Figure 10d–f) illuminate the synoptic conditions occurring before, during, and after the prolonged mixed-phase period during the event. At 0800 UTC, during the onset of the rain only period, we see that there is a low-pressure center to the east of the NWS MQT site with surface winds from the north (Figure 10a), while the 850 hPa temperatures are slightly above freezing (~2 °C) with winds from the northeast (Figure 10d). At the beginning of the mixed-phase precipitation period (1600 UTC), the low-pressure center moved slightly east and extended northeast (Figure 10b), and the 850 hPa temperatures cooled to below freezing (−2 °C) with winds continuing out of the northeast (Figure 10e). During the snow period starting at 0200 UTC on 25 October, the gradient of MSLP weakened and the low pressure is extended further to the northeast (Figure 10c), the 850 hPa temperatures continued to cool and are now −6 °C near the NWS MQT site (Figure 10f), and both the surface and 850 hPa winds shifted, originating from northwest of the site (Figure 10c,f). The slow progression of the low-pressure center eastward and cooling of the 850 hPa temperatures are consistent with the rain to mixed-phase to snowfall transition of the precipitation observed by the PIP. Additionally, this system appears to be occluded at the surface, with weak cold air advection in the lower levels (Figure 10d–f) that may have helped to promote the prolonged mixed-phase precipitation period seen during this event.
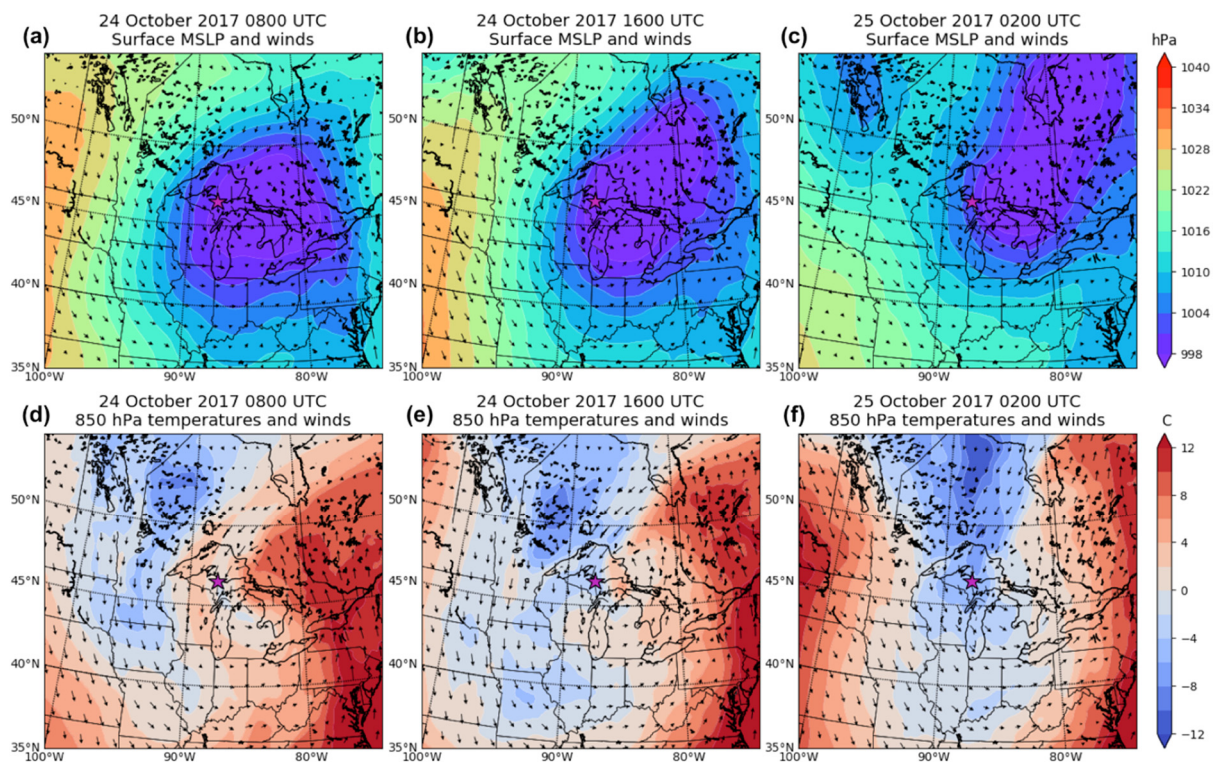
Figure 10. ERA5 MSLP and surface winds and 850 hPa temperatures and winds for 24 October 2017 0800 UTC (**a**,**d**) and 1600 UTC (**b**,**e**), and 25 October 2017 0200 UTC (**c**,**f**).

The observations from the NWS MQT office WSR-88D yield additional insight into the precipitation characteristics. Figure 11 shows radar reflectivity, Z_{DR}, and ρ_{HV} during the event, to highlight precipitation features during the rain, mixed-phase, and snowfall periods of the event. At 0805 UTC on 24 October 2017, the WSR-88D shows extensive large reflectivities (30 to 40 dBZ) in the NWS MQT region (Figure 11a). There are also relatively large values of Z_{DR} (Figure 11b) and low ρ_{HV} (Figure 11c) concentrically at distances >20 km from the NWS MQT site. These values indicate the approximate region of the mixed ice and rain precipitation and melting level, which correspond to heights >0.5 km AGL. This reasonably agrees with the MRR profile indication of melting levels around 1 km AGL (Figure 9a,b) and indicates that the precipitation is rain phase at the surface, consistent with the PIP precipitation phase identification (Figure 9d). At 1600 UTC, the WSR-88D reflectivities are very large (>40 dBZ) within the 15 km adjacent to the NWS MQT (Figure 11d). Additionally, there are large Z_{DR} (Figure 11e) and low ρ_{HV} (Figure 11f) values in the same region. This implies that the mixed-phase precipitation layer is very close to the surface, matching the observations seen at the surface by the PIP. At 0204 UTC on 25 October 2017, the WSR-88D observations suggest the presence of convective, possibly lake-effect snowfall at the NWS MQT site, with relatively small Z_{DR} and high ρ_{HV} values throughout the observing area (Figure 11g–i). The observations of precipitation characteristics from the WSR-88D agree with the progression of rain, to mixed-phase precipitation, to snowfall seen by the PIP and ancillary observations.
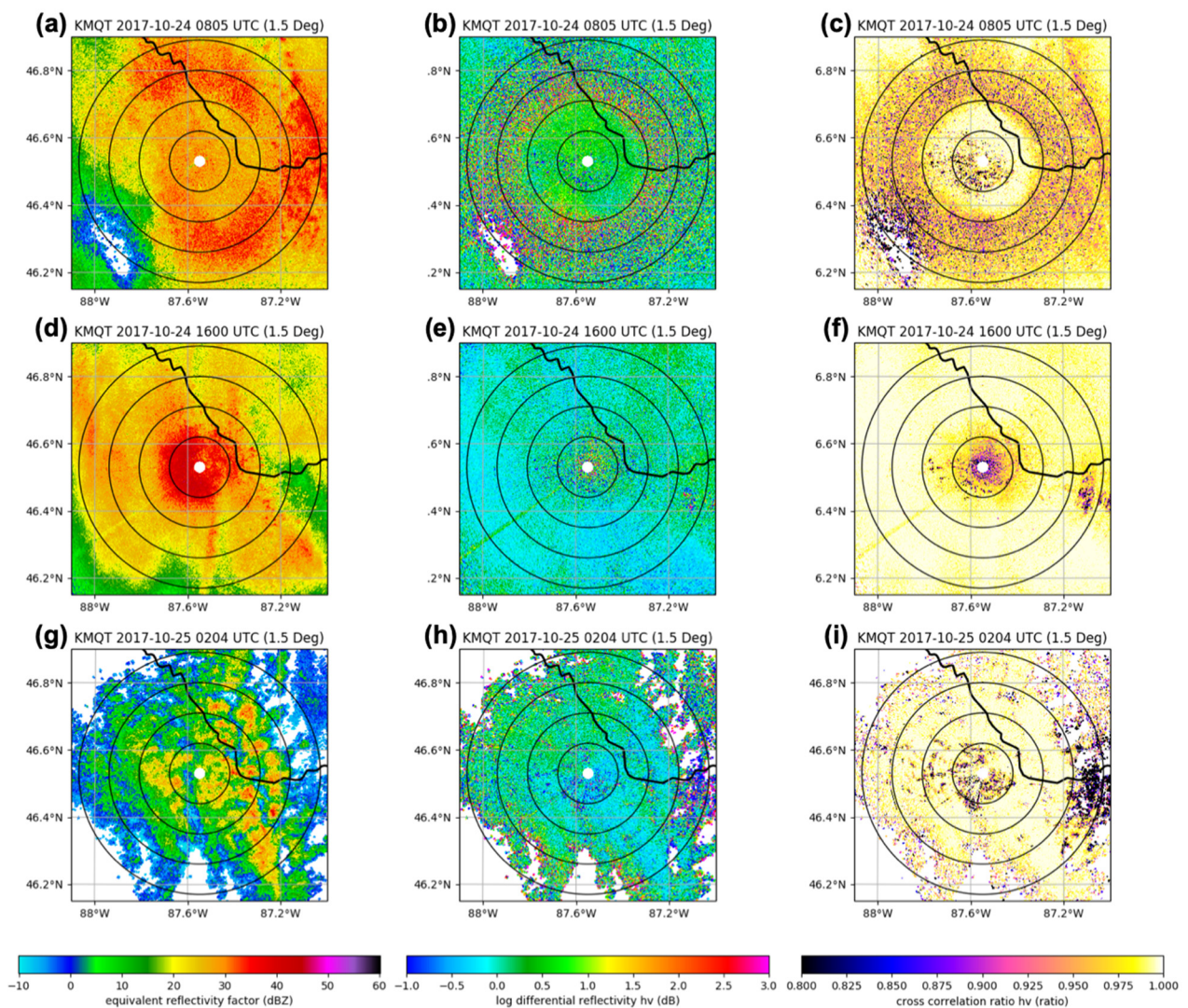
Figure 11. WSR-88D values of reflectivity, differential reflectivity (Z_{DR}), and cross correlation ratio (ρ_{HV}) for 24 October 2017 0805 UTC (**a**–**c**) and 1600 UTC (**d**–**f**), and 25 October 2017 0204 UTC (**g**–**i**).

Finally, profiles of temperature and relative humidity from the ERA5 reanalysis are examined for the rain, mixed-phase precipitation, and snowfall periods of the event. Figure 12a shows the temperature profiles for 24 October 2017 at 0800 UTC and 1600 UTC, and 25 October at 0200 UTC. During the rain period (solid line), profile temperatures throughout the boundary layer are quite warm and the near-surface temperature is >10 °C. During both the mixed-phase (dashed) and the snowfall (dotted) periods the near-surface temperatures are >0 °C. All three temperature profiles indicate an inversion around 800 hPa. The profiles of relative humidity (Figure 12b) do not vary much between the times, with the exception that at 24 October 0800 UTC the boundary layer is relatively dry, and at 25 October 0200 UTC that the free atmosphere is relatively dry. Again, the progression of the temperature profiles is consistent with the PIP observations of rain transitioning to mixed-phase precipitation and then finally to snowfall.
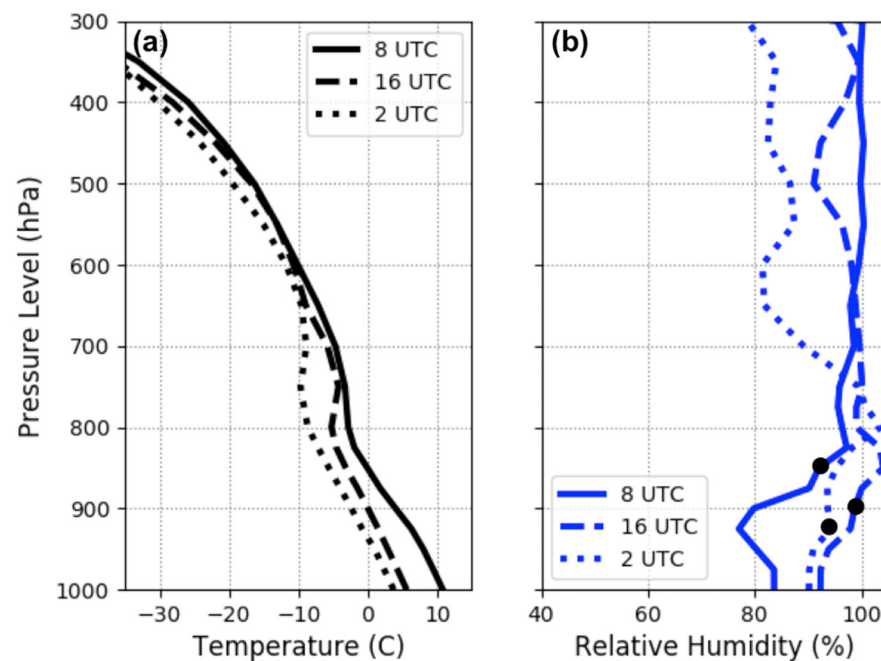
Figure 12. Profiles of temperature (**a**) and relative humidity (**b**) from the ERA5 reanalysis for 24 October 2017 0800 UTC (solid lines) and 1600 UTC (dashed lines), and 25 October 2017 0200 UTC (dotted lines). The black dots in panel b signify the 0 °C level for the profiles.

4. Discussion

There is considerable uncertainty in the ability of satellite observations to discriminate rain, varying degrees of mixed-phase, and snow precipitation. Current satellite-based radar profiles detect reflectivities from precipitation, but there is no inherent measurement that yields precipitation phase with high certainty. Similar to the profiles from the MRR and spatial distribution from the WSR-88D, the abrupt transition to higher values of reflectivity (i.e., "bright band") is often associated with the melting of ice and snow within the atmosphere, and can reflect the presence of rain at the surface [45–47]. However, the satellite radar "blind zone" affects the ability to distinguish precipitation phase when melting layers are located within 1 to 2 km AGL [15–17]. Additionally, algorithms that use satellite microwave sensors provide precipitation estimates and rely on ancillary information, typically from model reanalyses, to classify phase [18]. To help improve estimates of precipitation phase at the surface, Sims and Liu [20] developed a parameterization using reanalysis values of 2 m temperature, relative humidity, and surface pressure to calculate the surface wet bulb temperature (WBT) and the near-surface (500 m AGL) vertical lapse rate (LR). These variables are used to assign conditional probabilities of solid precipitation at the surface. Here, we use the surface observations and reanalysis profiles to obtain values of WBT and near-surface LR (both 500 and 1000 m AGL), respectively, for the phase transition events examined in Section 3.2, and assess the probability of solid precipitation using the Sims and Liu [20] parameterization.

The event on 11 January 2018 transitioned from rain to mostly snow around 1630 UTC, at which point surface temperatures steadily decrease from 0 to −10 °C over the next 8 h. At 1500 UTC the PIP observes rain precipitation at the surface (Figure 3d) and the WBT is 1.2 °C and near-surface (500 m AGL) LR is 5 °C km^{-1} (positive LR values indicates temperature decreasing with height), which correspond to a probability of solid precipitation of 30% using the Sims and Liu [20] parameterization (see Table 4). There is a steady decrease in WBTs and increase in LRs between 1500 and 1900 UTC, leading to increased probability of snowfall (30% to 90%) during this period. The WBT drops to −2 °C at 1900 UTC at which point the LR is 6.4 °C km^{-1} and indicates a probability of solid precipitation >90%, while simultaneously the PIP observes mostly snowfall with trace amounts of mixed-phase

precipitation. At 2100 UTC, the PIP observed only snowfall for several hours and the WBT is constant at −6.5 °C, which is associated with a 100% probability of solid precipitation (effectively regardless of the near-surface LR). Notably, the LR values for 1000 m AGL were 1.5 to 8 °C km^{-1} less than those for 500 m AGL, which would generally correspond to a reduction in the likelihood of solid precipitation at the surface.

Table 4. Select times within each event with calculated wet bulb temperature (WBT) from surface observations and lapse rate (LR) from ERA5 reanalysis profiles. The WBT and LR are used to find a probability of solid precipitation via Sims and Liu [20] and compare to the precipitation phase as determined by the PIP. * Denotes +1 day UTC from start date.

Time	Wet Bulb (°C)	Lapse Rate (°C km^{-1})	Probability of Solid Precipitation	Precipitation Phase (PIP)
		11 January 2018		
1500 UTC	1.2	5.0	30%	Rain
1700 UTC	0.8	5.5	40%	Snow
1900 UTC	−2.0	6.4	>90%	Snow
2100 UTC	−6.5	8.8	100%	Snow
		21 November 2019		
1500 UTC	3.0	5.2	<10%	Rain
1800 UTC	0.2	6.2	>80%	Snow
		27 December 2018		
1200 UTC	−2.8	2.5	>90%	Snow
1800 UTC	−1.0	6.8	>90%	Rain
0000 UTC*	0.0	4.8	80%	Rain
0600 UTC*	1.0	3.1	30%	Rain
1800 UTC*	−7.0	10.0	100%	Snow
		24 October 2017		
0800 UTC	6.0	7.2	<10%	Rain
1600 UTC	2.0	6.5	10%	Rain
1800 UTC	1.8	6.5	10%	Mixed
2000 UTC	1.2	7.0	40%	Mixed
2200 UTC	0.8	7.2	60%	Mixed
0200 UTC *	0.0	7.5	80%	Snow

The 21 November 2019 precipitation event transitioned abruptly from rain to snowfall at 1650 UTC, corresponding to a rapid decline in observed surface temperatures from 3.5 to 0.5 °C starting at 1600 UTC (Figure 5g). During the rain period of the event, the WBTs were constant at 3 °C with near-surface LRs of ~5.2 °C km^{-1}, which correspond to <10% likelihood of solid precipitation (Table 4). At 1800 UTC the PIP observations indicated snowfall for >1 h and the WBT is 0.2 °C and LR 6.2 °C km^{-1}, which correspond to a probability of solid precipitation >80%. Again, there is a difference between the LRs calculated at 500 versus 1000 m AGL, with the latter having values 2 °C km^{-1} lower, which would reduce the probability of solid precipitation to ~70% during the snowfall period of the event.

The precipitation event on 27 December 2018 featured two phase transitions: snow-to-rain at approximately 2000 UTC, and rain-to-snow on 28 December at 1015 UTC (Figure 7d). At 1200 UTC on 27 December, the WBT was −2.8 °C and the near-surface LR was 2.5 °C km^{-1}, predicting a >90% likelihood of solid precipitation, which corresponds to the PIP indicated snowfall at that time (Table 4). The PIP indicated sporadic rain between 2000 UTC and 1000 UTC (28 December), with trends of WBT from 0 and 2 °C and LRs from 4.8 to 3 °C km^{-1}. The probability of solid precipitation was therefore 80% at the onset of the rain, <10% at the highest WBT, and 30% towards the end of the rainfall period. The surface temperature rapidly decreased starting at 0800 UTC (28 December) and continued to drop. The decrease coincided with reduced WBTs and probabilities of solid precipitation

of >90% by 1200 UTC, which were consistent with the PIP observations of snowfall from 1015 UTC onward. As with the two previously discussed events, the LRs calculated 1000 m AGL have values 2 to 4 °C km^{-1} smaller than those at 500 m AGL, which would reduce the probabilities of solid precipitation during the rain period of the event by about 20%.

Finally, we examine the prolonged mixed-phase precipitation event on 24 October 2017, with a period of transitioning precipitation from approximately 1600 to 2200 UTC (Figure 9d). During the rain period of the event, the WBTs decreased from 7 °C at 0600 UTC to 2 °C at 1600 UTC, while LRs over the same period ranged from 7.2 to 6.50 °C km^{-1}, indicating 10% likelihood of solid precipitation (Table 4). Simultaneous with the onset of the mixed-precipitation at 1600 UTC, the WBTs slowly decreased from 2 to 0.8 °C (at 2200 UTC) and LRs increased from 6.5 to 7.2 °C km^{-1}. The mixed-phase period corresponded to a probability of solid precipitation of 10% at the beginning and steadily increased to 60% by 2200 UTC. The PIP observations indicate mostly snowfall by 0200 UTC on 28 October, at which time the WBT is 0 °C and LR is 7.5 °C km^{-1}, which corresponds to a probability of solid precipitation of ~80%. Unlike the other events examined, there were little to no differences in the LR values at 500 m and 1000 m AGL.

The probabilities of solid precipitation per the Sims and Liu [20] parameterization largely agree with the PIP observations of surface precipitation phase during the example events. Additionally, the trends in probabilities (increase/decrease) align with the observations, even during complicated multiple phase transition and prolonged mixed-phase precipitation events.

5. Conclusions

The 13 events examined illustrate the ability of the PIP instrument to accurately distinguish precipitation phases, including mixed-phase conditions with simultaneous liquid and non-liquid hydrometeors. The PIP has excellent agreement with the NWS MQT forecaster reports of the timing of precipitation phase changes, with the majority of event onsets and endings within 15 min. The PIP and NWS MQT event LWE accumulation were within 10%, with the exception of the 24 October 2017, which contained an unusually long period of mixed-phase precipitation, was by far the highest wind speeds of any event. Additionally, the PIP observations are at very high-temporal resolution (1 min) and can therefore resolve abrupt changes in precipitation phase. The four precipitation transition events that were investigated in detail indicate that the PIP phase identification is accurate. The PIP-determined precipitation phase observations are supported through investigation of co-located observations from the Parsivel, MRR, and WSR-88D, and from ERA5 reanalysis products such as profiles of temperature and relative humidity and spatial information from MSLP, 850 hPa temperatures, and winds.

The PIP precipitation phase identification compared well to the Sims and Liu [20] parameterization output of the probability of solid precipitation. The PIP precipitation phase information can be used to assess and validate parameterization schemes such as demonstrated here. Further, the PIP observations could be leveraged to improve and refine parameterizations, which would subsequently improve satellite remote sensing products that utilize the outputs to inform their retrievals of precipitation. Additionally, deployment of the PIP instrument with co-located ground-based scanning (e.g., WSR-88D) or profiling (e.g., MRR) radars could help assess precipitation phase gleaned from remote sensing observations. This would be especially useful for phase transitions occurring very close to the surface or during mixed-phase precipitation.

References

1. Uccellini, L.W.; Kocin, P.J. The interaction of jet streak circulations during heavy snow events along the east coast of the United States. *Weather Forecast.* **1987**, *2*, 289–308. [CrossRef]
2. Kocin, P.J.; Schumacher, P.N.; Morales, R.F., Jr.; Uccellini, L.W. Overview of the 12–14 March 1993 superstorm. *Bull. Am. Meteorol. Soc.* **1995**, *76*, 165–182. [CrossRef]
3. Maglaras, G.J.; Waldstreicher, J.S.; Kocin, P.J.; Gigi, A.F.; Marine, R.A. Winter weather forecasting throughout the eastern United States. Part I: An overview. *Weather Forecast.* **1995**, *10*, 5–20. [CrossRef]
4. Uccellini, L.W.; Kocin, P.J.; Schneider, R.S.; Stokols, P.M.; Dorr, R.A. Forecasting the 12–14 March 1993 superstorm. *Bull. Am. Meteorol. Soc.* **1995**, *76*, 183–200. [CrossRef]
5. Keeter, K.K.; Businger, S.; Lee, L.G.; Waldstreicher, J.S. Winter weather forecasting throughout the eastern United States. Part III: The effects of topography and the variability of winter weather in the Carolinas and Virginia. *Weather Forecast.* **1995**, *10*, 42–60. [CrossRef]
6. Musselman, K.N.; Lehner, F.; Ikeda, K.; Clark, M.P.; Prein, A.F.; Liu, C.; Barlage, M.; Rasmussen, R. Projected increases and shifts in rain-on-snow flood risk over western North America. *Nat. Clim. Chang.* **2018**, *8*, 808–812. [CrossRef]
7. Suriano, Z.J.; Leathers, D.J.; Benjamin, A.E. Regionalization of Northeast US moisture conditions: Analysis of synoptic-scale atmospheric drivers. *Clim. Res.* **2020**, *79*, 193–206. [CrossRef]
8. Li, Q.; Yang, T.; Zhou, H.; Li, L. Patterns in snow depth maximum and snow cover days during 1961–2015 period in the Tianshan Mountains, Central Asia. *Atmos. Res.* **2019**, *228*, 14–22. [CrossRef]
9. Wachowicz, L.J.; Mote, T.L.; Henderson, G.R. A rain on snow climatology and temporal analysis for the eastern United States. *Phys. Geogr.* **2020**, *41*, 54–69. [CrossRef]
10. Arigony-Neto, J.; Saurer, H.; Simões, J.C.; Rau, F.; Jaña, R.; Vogt, S.; Gossmann, H. Spatial and temporal changes in dry-snow line altitude on the Antarctic Peninsula. *Clim. Chang.* **2009**, *94*, 19–33. [CrossRef]
11. Hantel, M.; Maurer, C.; Mayer, D. The snowline climate of the Alps 1961–2010. *Theor. Appl. Climatol.* **2012**, *110*, 517–537. [CrossRef]
12. Fabry, F.; Zawadzki, I. Long-term radar observations of the melting layer of precipitation and their interpretation. *J. Atmos. Sci.* **1995**, *52*, 838–851. [CrossRef]
13. Vivekanandan, J.; Zrnic, D.S.; Ellis, S.M.; Oye, R.; Ryzhkov, A.V.; Straka, J. Cloud microphysics retrieval using S-band dual-polarization radar measurements. *Bull. Am. Meteorol. Soc.* **1999**, *80*, 381–388. [CrossRef]
14. Lim, J.O.J.; Hong, S.Y. Effects of bulk ice microphysics on the simulated monsoonal precipitation over East Asia. *J. Geophys. Res. Atmos.* **2005**, *110*. [CrossRef]
15. Maahn, M.; Burgard, C.; Crewell, S.; Gorodetskaya, I.V.; Kneifel, S.; Lhermitte, S.; Van Tricht, K.; van Lipzig, N.P. How does the spaceborne radar blind zone affect derived surface snowfall statistics in polar regions? *J. Geophys. Res. Atmos.* **2014**, *119*, 13–604. [CrossRef]

16. Norin, L.; Devasthale, A.; L'Ecuyer, T.S.; Wood, N.B.; Smalley, M. Intercomparison of snowfall estimates derived from the CloudSat Cloud Profiling Radar and the ground-based weather radar network over Sweden. *Atmos. Meas. Tech.* **2015**, *8*, 5009–5021. [CrossRef]

17. Casella, D.; Panegrossi, G.; Sanò, P.; Marra, A.C.; Dietrich, S.; Johnson, B.T.; Kulie, M.S. Evaluation of the GPM-DPR snowfall detection capability: Comparison with CloudSat-CPR. *Atmos. Res.* **2017**, *197*, 64–75. [CrossRef]

18. Kummerow, C.D.; Randel, D.L.; Kulie, M.; Wang, N.Y.; Ferraro, R.; Joseph Munchak, S.; Petkovic, V. The evolution of the Goddard profiling algorithm to a fully parametric scheme. *J. Atmos. Ocean. Technol.* **2015**, *32*, 2265–2280. [CrossRef]

19. Zhang, J.; Howard, K.; Langston, C.; Vasiloff, S.; Kaney, B.; Arthur, A.; Van Cooten, S.; Kelleher, K.; Kitzmiller, D.; Ding, F.; et al. National Mosaic and Multi-Sensor QPE (NMQ) system: Description, results, and future plans. *Bull. Am. Meteorol. Soc.* **2011**, *92*, 1321–1338. [CrossRef]

20. Sims, E.M.; Liu, G. A parameterization of the probability of snow–rain transition. *J. Hydrometeorol.* **2015**, *16*, 1466–1477. [CrossRef]

21. Burdanowitz, J.; Klepp, C.; Bakan, S. An automatic precipitation-phase distinction algorithm for optical disdrometer data over the global ocean. *Atmos. Meas. Tech.* **2016**, *9*, 1637–1652. [CrossRef]

22. Kochendorfer, J.; Nitu, R.; Wolff, M.; Mekis, E.; Rasmussen, R.; Baker, B.; Earle, M.E.; Reverdin, A.; Wong, K.; Smith, C.D.; et al. Testing and development of transfer functions for weighing precipitation gauges in WMO-SPICE. *Hydrol. Earth Syst. Sci.* **2018**, *22*, 1437. [CrossRef]

23. Rasmussen, R.; Baker, B.; Kochendorfer, J.; Meyers, T.; Landolt, S.; Fischer, A.P.; Black, J.; Thériault, J.M.; Kucera, P.; Gochis, D.; et al. How well are we measuring snow: The NOAA/FAA/NCAR winter precipitation test bed. *Bull. Am. Meteorol. Soc.* **2012**, *93*, 811–829. [CrossRef]

24. Löffler-Mang, M.; Joss, J. An optical disdrometer for measuring size and velocity of hydrometeors. *J. Atmos. Ocean. Technol.* **2000**, *17*, 130–139. [CrossRef]

25. Wayand, N.E.; Stimberis, J.; Zagrodnik, J.P.; Mass, C.F.; Lundquist, J.D. Improving simulations of precipitation phase and snowpack at a site subject to cold air intrusions: Snoqualmie Pass, WA. *J. Geophys. Res. Atmos.* **2016**, *121*, 9929–9942. [CrossRef]

26. Tokay, A.; Wolff, D.B.; Petersen, W.A. Evaluation of the new version of the laser-optical disdrometer, OTT Parsivel2. *J. Atmos. Ocean. Technol.* **2014**, *31*, 1276–1288. [CrossRef]

27. Dolan, B.; Fuchs, B.; Rutledge, S.A.; Barnes, E.A.; Thompson, E.J. Primary modes of global drop size distributions. *J. Atmos. Sci.* **2018**, *75*, 1453–1476. [CrossRef]

28. Park, S.G.; Kim, H.L.; Ham, Y.W.; Jung, S.H. Comparative evaluation of the OTT PARSIVEL2 using a collocated two-dimensional video disdrometer. *J. Atmos. Ocean. Technol.* **2017**, *34*, 2059–2082. [CrossRef]

29. Battaglia, A.; Rustemeier, E.; Tokay, A.; Blahak, U.; Simmer, C. PARSIVEL snow observations: A critical assessment. *J. Atmos. Ocean. Technol.* **2010**, *27*, 333–344. [CrossRef]

30. Newman, A.J.; Kucera, P.A.; Bliven, L.F. Presenting the snowflake video imager (SVI). *J. Atmos. Ocean. Tech.* **2009**, *26*, 167–179. [CrossRef]

31. Pettersen, C.; Bliven, L.F.; von Lerber, A.; Wood, N.B.; Kulie, M.S.; Mateling, M.E.; Moisseev, D.N.; Munchak, S.J.; Petersen, W.A.; Wolff, D.B. The Precipitation Imaging Package: Assessment of Microphysical and Bulk Characteristics of Snow. *Atmosphere* **2020**, *11*, 785. [CrossRef]

32. Pettersen, C.; Kulie, M.S.; Bliven, L.F.; Merrelli, A.J.; Petersen, W.A.; Wagner, T.J.; Wolff, D.B.; Wood, N.B. A composite analysis of snowfall modes from four winter seasons in Marquette, Michigan. *J. Appl. Meteorol. Climatol.* **2020**, *59*, 103–124. [CrossRef]

33. Kulie, M.S.; Pettersen, C.; Merrelli, A.J.; Wagner, T.J.; Wood, N.B.; Dutter, M.; Beachler, D.; Kluber, T.; Turner, R.; Mateling, M.; et al. Snowfall in the Northern Great Lakes: Lessons Learned from a Multi-Sensor Observatory. *Bull. Am. Meteorol. Soc.* **2021**, 1–61. [CrossRef]

34. Hou, A.Y.; Kakar, R.K.; Neeck, S.; Azarbarzin, A.A.; Kummerow, C.D.; Kojima, M.; Oki, R.; Nakamura, K.; Iguchi, T. The global precipitation measurement mission. *Bull. Am. Meteorol. Soc.* **2014**, *95*, 701–722. [CrossRef]

35. von Lerber, A.; Moisseev, D.; Bliven, L.F.; Petersen, W.; Harri, A.M.; Chandrasekar, V. Microphysical properties of snow and their link to Z e–S relations during BAECC 2014. *J. Appl. Meteor. Clim.* **2017**, *56*, 1561–1582. [CrossRef]

36. Klugmann, D.; Heinsohn, K.; Kirtzel, H.J. A low cost 24 GHz FM-CW Doppler radar rain profiler. *Contrib. Atmos. Phys.* **1996**, *61*, 247–253.

37. Peters, G.; Fischer, B.; Andersson, T. Rain observations with a vertically looking Micro Rain Radar (MRR). *Boreal Environ. Res.* **2002**, *7*, 353–362.

38. Kneifel, S.; Maahn, M.; Peters, G.; Simmer, C. Observation of snowfall with a low-power FM-CW K-band radar (Micro Rain Radar). *Meteorol. Atmos. Phys.* **2011**, *113*, 75–87. [CrossRef]

39. Maahn, M.; Kollias, P. Improved Micro Rain Radar snow measurements using Doppler spectra post-processing. *Atmos. Meas. Tech.* **2012**, *5*, 2661–2673. [CrossRef]

40. Stull, R. Wet-bulb temperature from relative humidity and air temperature. *J. Appl. Meteorol. Climatol.* **2011**, *50*, 2267–2269. [CrossRef]

41. Hersbach, H.; Bell, B.; Berrisford, P.; Hirahara, S.; Horányi, A.; Muñoz-Sabater, J.; Nicolas, J.; Peubey, C.; Radu, R.; Schepers, D.; et al. The ERA5 global reanalysis. *Q. J. R. Meteorol. Soc.* **2020**, *146*, 1999–2049. [CrossRef]

42. Atlas, D.; Ulbrich, C.W. Path-and area-integrated rainfall measurement by microwave attenuation in the 1–3 cm band. *J. Appl. Meteorol.* **1977**, *16*, 1322–1331. [CrossRef]

43. Heymsfield, A.J.; Bansemer, A.; Schmitt, C.; Twohy, C.; Poellot, M.R. Effective ice particle densities derived from aircraft data. *J. Atmos. Sci.* **2004**, *61*, 982–1003. [CrossRef]
44. Herzegh, P.H.; Jameson, A.R. Observing precipitation through dual-polarization radar measurements. *Bull. Am. Meteorol. Soc.* **1992**, *73*, 1365–1376. [CrossRef]
45. Ryzhkov, A.V.; Zrnic, D.S. Discrimination between rain and snow with a polarimetric radar. *J. Appl. Meteorol.* **1998**, *37*, 1228–1240. [CrossRef]
46. Matrosov, S.Y. Modeling backscatter properties of snowfall at millimeter wavelengths. *J. Atmos. Sci.* **2007**, *64*, 1727–1736. [CrossRef]
47. Austin, P.M.; Bemis, A.C. A quantitative study of the "bright band" in radar precipitation echoes. *J. Atmos. Sci.* **1950**, *7*, 145–151. [CrossRef]